



Electronic properties and carrier transport properties of low-dimensional aluminium doped silicene nanostructure

Chuan Mu Wen, Wong Kien Liong, Hamzah Afiq, Rusli Shahrizal, Alias Nurul Ezaila, Lim Cheng Siong, Tan Michael Loong Peng^{*}

School of Electrical Engineering, Faculty of Engineering, Universiti Teknologi Malaysia, 81310 Skudai, Johor, Malaysia

ARTICLE INFO

Keywords:

Doped silicene
Carrier statistics
Intrinsic velocity
Carrier transport
I-V characteristics

ABSTRACT

Unlike graphene which requires redesigned fabrication technique, silicene is predicted to be compatible with the silicon wafer technology. However, similar to graphene, the gapless properties of silicene hinder its application as field-effect transistors (FETs). By employing nearest neighbour tight-binding (NNTB) approach and Landauer-Büttiker formalism, the analytical equations for electronic band structure, density of states (DOS), intrinsic carrier concentration, intrinsic velocity and ideal ballistic I-V characteristics have been derived. The simulated results using MATLAB show that a band gap of 0.78 eV has been induced in uniformly doped silicene with aluminium (AlSi₃NW) in the zigzag direction. The device performance metrics extracted from the current-voltage (I-V) characteristics are subthreshold swing of 60 mV/decade and threshold voltage of 0.65 V under ideal conditions at room temperature. The results indicate that AlSi₃NW device possesses good channel control and effective switching behaviour. The proposed model demonstrates that AlSi₃NW is a potential candidate for future nanoelectronic applications.

1. Introduction

As the semiconducting industry is entering post-Moore's Law era [1], research featuring two-dimensional (2D) materials for nanoelectronic applications have become an emerging topic [2]. Moreover, nanosheet field-effect transistor (FET) is envisaged to be the final resort for transistor sizing [3]. Driven by graphene which is the first 2D material available physically [4,5], increasing number of theoretical and experimental literatures associated with other 2D materials have become available [6,7]. Silicene is one of the 2D materials beyond graphene which consists of silicon (Si) atoms arranged in graphene-like lattice structure. Interestingly, silicene is included as one of the "More than Moore" materials for transistor scaling in International Roadmap for Devices and Systems (IRDS) [8]. Theoretical prediction of silicene has been reported in 1994 using density functional theory (DFT) [9] and later verified by first-principles calculations [10] and tight-binding (TB) model [11]. Recently, experimental formation of silicene on various surfaces [12–16] has also been carried out but the fabrication of free-standing silicene has not yet been discovered [17].

As an analogous structure to graphene, silicene exhibits similar Dirac cones property which results in ultra-high carrier mobility. This

extraordinary property can be observed in the electronic band structure as shown in Fig. 1 where the conduction band and valence band of pristine silicene crosses each other at the K-point within the first Brillouin zone. This phenomena has also been proven experimentally [13]. Despite the fact that silicene can be compatible with recent Si fabrication technology [18], the gapless property of silicene hinders its application as FETs which require the channel materials to possess the values of band gap between 0.1 eV [19] and 3 eV [20] such that on- and off-states of the devices can be effectively differentiated.

To overcome the gapless shortcoming of silicene, various band gap engineering techniques have been proposed and explored. For instance, electronic properties of silicene featuring finite nanoribbon sizes [22–24], point vacancy defects [25–29], line edge modifications [30, 31], substitutional doping [32–36], strain engineering [37–40], surface functionalization [41–43] and other techniques have been investigated. Among the mentioned techniques, substitutional doping is a well-established approach in the semiconductor industry to design a logic circuit [44]. In addition, Ding et al. [36] have observed useful band gap values in silicene by applying substitutional doping with aluminium (Al) at uniform concentration, namely the 2D AlSi₃ structure. The primary advantage of using Al as the dopant is that it retains the perfect

^{*} Corresponding author.

E-mail address: michael@utm.my (M.L.P. Tan).

<https://doi.org/10.1016/j.physe.2019.113731>

Received 31 August 2019; Received in revised form 15 September 2019; Accepted 17 September 2019

Available online 18 September 2019

1386-9477/© 2019 Elsevier B.V. All rights reserved.

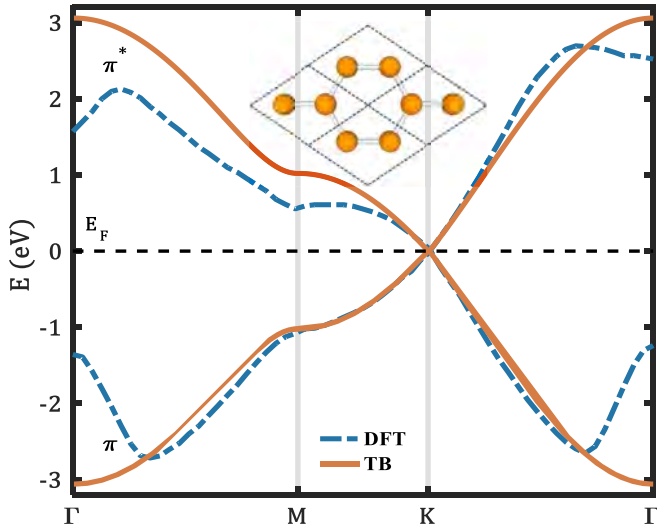


Fig. 1. The band structure of pristine silicene where the blue dashed line and red solid line represents results of DFT calculation adapted from Ref. [21] and TB approach respectively; the black dashed parallelogram displays the 2×2 silicene supercell. (For interpretation of the references to colour in this figure legend, the reader is referred to the Web version of this article.)

honeycomb lattice arrangement with the lattice constant, a of 8.11 Å [36]. Although the proposed structure has successfully opened the band gap of silicene to a useful semiconducting value, but there is still lack of detailed investigation on the important parameters of 2D AlSi_3 for the current-to-voltage (I-V) characteristics such as the carrier concentration, intrinsic velocity and drift current.

In the view of these shortcomings, an analytical modelling based on the parabolic band assumption is proposed in this work to obtain the important parameters of one-dimensional (1D) AlSi_3 nanowire (AlSi_3NW) in the zigzag direction as shown in Fig. 2 for electronic and carrier transport properties. The key advantage of this approach is that simple and comprehensive analytical equations can be obtained. The remaining of the paper is organized as follows. In Section 2, the modelling and simulation of band structure and density of states (DOS) of AlSi_3NW based on nearest neighbour tight-binding approach (NNTB) and parabolic band assumption is shown, followed by the analysis of carrier concentrations within the degenerate and non-degenerate regimes. In Section 3, intrinsic velocity is calculated and its relationships with the carrier concentrations and temperature are analysed. Based on these parameters, Landauer-Büttiker formalism is applied to obtain the I-V characteristic at high drain bias. In Section 4, the performance of AlSi_3NW is benchmarked and discussed. Finally, the conclusion and future recommendations are drawn in Section 5.

2. Mathematical modelling for carrier statistics

2.1. Band structure and density of states of AlSi_3NW

Fig. 2 depicts the schematic lattice structure of the 2D AlSi_3 with the corresponding displacement vectors to its nearest neighbours, namely \vec{a}_1 and \vec{a}_2 . The structure is assumed to be in perfect planar [36] honeycomb lattice structure (120° each interior angle). Each unit cell will interact with 4 nearest neighbours, however, the other two displacement vectors are just the complex conjugate of \vec{a}_1 and \vec{a}_2 . To apply the NNTB, the matrix form time-independent Schrödinger equation is applied [45], given as

$$E(\phi_0) = [h(\vec{k})](\phi_0) \quad (1)$$

where E is the energy, ϕ_0 is the wave function and $[h(\vec{k})]$ is the matrix

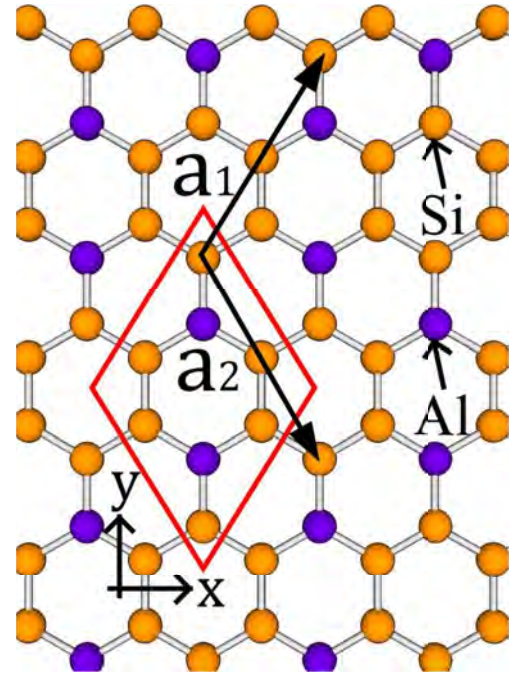


Fig. 2. The schematic diagram of 2D AlSi_3 where the brown and blue atoms are the silicon (Si) and aluminium (Al) atoms respectively; \vec{a}_1 and \vec{a}_2 are the displacement vectors; the red parallelogram depicts the single primitive unit cell of the material. (For interpretation of the references to colour in this figure legend, the reader is referred to the Web version of this article.)

representation of Hamiltonian operator. The Hamiltonian operator matrix is computed by summing all non-zero overlap components as the positive integer, m runs over all nearest neighbouring unit cells using

$$[h(\vec{k})] = \sum_{m=1,n} H_{nm} e^{i\vec{k} \cdot (\vec{r}_n - \vec{r}_m)} \quad (2)$$

where \vec{k} is the wave vector, H_{nm} is the Hamiltonian matrix for each unit cell, \vec{r}_n and \vec{r}_m are the position vectors which define the displacement of m^{th} unit cell with respect to the n^{th} unit cell. The origin can be fixed at any one of the atoms of the within the n^{th} unit cell. In this work, the n^{th} unit cell is defined as the enclosed unit cell in the red parallelogram as shown in Fig. 2. By computing the unit cell Hamiltonian matrices, namely H_{nn} , H_{n1} , H_{n2} , H_{n3} , H_{n4} and expanding (2), the complete matrix equation is computed as

$$[h(\vec{k})] = \begin{bmatrix} E_{oSi} & 0 & 0 & t_{Al-Si} & 0 & h_1^* & h_2^* & 0 \\ 0 & E_{oSi} & 0 & t_{Al-Si} & 0 & 0 & t_{Si-Si} & h_1^* \\ 0 & 0 & E_{oSi} & t_{Al-Si} & 0 & t_{Si-Si} & 0 & h_2^* \\ t_{Al-Si} & t_{Al-Si} & t_{Al-Si} & E_{oAl} & 0 & 0 & 0 & 0 \\ 0 & 0 & 0 & 0 & E_{oAl} & t_{Al-Si} & t_{Al-Si} & t_{Al-Si} \\ h_1 & 0 & t_{Si-Si} & 0 & t_{Al-Si} & E_{oSi} & 0 & 0 \\ h_2 & t_{Si-Si} & 0 & 0 & t_{Al-Si} & 0 & E_{oSi} & 0 \\ 0 & h_1 & h_2 & 0 & t_{Al-Si} & 0 & 0 & E_{oSi} \end{bmatrix} \quad (3)$$

where $h_1 = t_{Si-Si} e^{i(ak_x - bk_y)}$ and $h_2 = t_{Si-Si} e^{i(ak_x + bk_y)}$. E_{oSi} and E_{oAl} is the on-site energy for Si and Al atom respectively, $t_{Al-Si} = t_{Si-Al}$ is the hopping integral for Al-Si (or Si-Al) atoms and t_{Si-Si} is the hopping integral for Si-Si atoms. h_1^* and h_2^* is the complex conjugate of h_1 and h_2 respectively. The influence of foreign atoms (Al) to the Hamiltonian matrix of silicene is highlighted in bold font as shown in (3).

The values of the tight-binding parameters are: $t_{Si-Si} = -1.02$ eV,

$t_{Al-Si} = -1.05$ eV, $E_{OSi} = -7.59$ eV [46] and $E_{oAl} = -5.71$ eV [46]. After that, confinement technique is applied to y-direction [47] to obtain 1D AlSi₃NW in the zigzag direction. Then, (3) is substituted into (1) to obtain the standard eigenvalue problem equation. Although analytical solution is possible for 8×8 matrix, the obtained characteristic equations will consist of 8th order polynomials which are not meaningful to be written. Hence, the standard eigenvalue problem is solved numerically using the equation: $\det[h(\vec{k})] - EI = 0$ to obtain the energy eigenvalues. Fig. 3 illustrates the band structure of AlSi₃NW. By comparing Figs. 1 and 3, it is observed uniform doping with Al is proven to effectively induce a semiconducting band gap value ($E_g \approx 0.78$ eV) in the gapless silicene. This band gap value is in consistent with previous DFT study [36] although the overall trends of the conduction band and valence band do not show exact fit. Considering that the band gap value is now between 0.1 eV and 3 eV, the AlSi₃NW structure is suitable to be applied in FET devices.

In order to obtain simple analytical model for current transport in nanoscale metal-oxide-semiconductor FET (MOSFET) [48], parabolic assumption is employed around the conduction band minimum (CBM) and valence band maximum (VBM) [49] because these are the bands that are responsible for carrier flow in most of the semiconductor devices. The parabolic band assumption originates from the effective mass equations such that the wave functions in the Schrödinger equation do not appear explicitly [50] to simplify the modelling procedures, the parabolic band equations are given as

$$E_e(k) = E_c + \frac{\hbar^2 k^2}{2m_e^*} \quad (4a)$$

$$E_h(k) = E_v + \frac{\hbar^2 k^2}{2m_h^*} \quad (4b)$$

where E_c and E_v are the energies at CBM and VBM respectively; $\hbar = h/(2\pi)$ is the Planck's constant. The effective mass for electron and hole are found to be $m_e^* = 0.235m_0$ and $m_h^* = 0.255m_0$ respectively where m_0 is the constant for electron rest mass.

The DOS for electron and hole can then be derived by applying the parabolic band equations (4a) and (4b). The DOS which describes the number of available states with respect to energy E is derived using the expression [51], given by

$$DOS(E) = \frac{\Delta N_x}{L_x \Delta E} \quad (5)$$

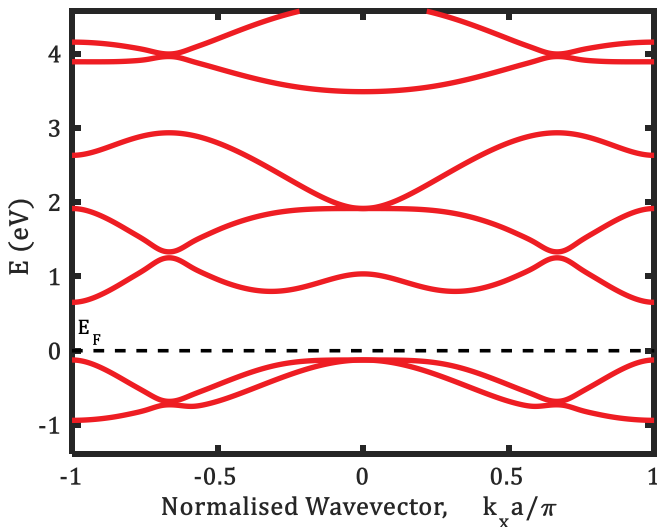


Fig. 3. The band structure of AlSi₃NW in the zigzag direction using NNTB model.

where N_x is the total number of states, L_x is the length and E is the energy. The resulting DOS for electrons and holes are obtained as

$$DOS_e(E) = \sqrt{\frac{2m_e^*}{\pi^2 \hbar^2}} (E - E_c)^{-1/2} \quad (6a)$$

$$DOS_h(E) = \sqrt{\frac{2m_h^*}{\pi^2 \hbar^2}} (E_v - E)^{-1/2} \quad (6b)$$

where the DOS for electron, DOS_e is derived using (4a) and DOS for hole, DOS_h is derived using (4b). Fig. 4(a) depicts the nicely fitted parabolic band structure around the CBM and VBM of AlSi₃NW and Fig. 4(b) depicts the DOS plotted using (6a) and (6b). It is shown that the peaks of the DOS occur at the energy levels of CBM and VBM. Since the height of the peaks depends on the effective masses of electrons and holes, the peak for DOS_e is higher than that for DOS_h . As expected, the Fermi energy level which is set to zero, is closer to the valence band, indicating that Al atoms have induced p-type doping in silicene.

2.2. Carrier concentration of AlSi₃NW

This subsection describes the derivation of the electrons and holes concentrations available in the conduction band and valence band respectively. The probability of the occupied states at a given temperature, T can be described by Fermi-Dirac distribution [52], given by

$$f(E) = \left[1 + \exp\left(\frac{E - E_F}{k_B T}\right) \right]^{-1} \quad (7)$$

where k_B is the Boltzmann constant. The thermal equilibrium (intrinsic) electrons concentration [53] in the conduction band is calculated using

$$n = \int_0^\infty DOS_e(E) f(E) dE = N_c \mathfrak{F}_{-1/2}(\eta_c) \quad (8)$$

where $\mathfrak{F}_{-1/2}(\eta_c)$ is the Fermi-Dirac integral (FDI) of order $-1/2$ with respect to η_c ; the effective DOS of electrons, N_c and normalised energy in terms of thermal energy, η_c is given by $N_c = \sqrt{(2m_e^* k_B T)/\pi \hbar^2}$ and $\eta_c = (E_F - E_c)/k_B T$ respectively. The general equation for FDI of order j [54] is given by

$$\mathfrak{F}_j(\eta) \equiv \frac{1}{\Gamma(j+1)} \int_0^\infty \frac{e^{\eta} d\epsilon}{1 + e^{\epsilon - \eta}} \quad (9)$$

where Γ is the gamma function. (9) is an important equation and will be used extensively hereafter. Similarly, the intrinsic holes concentration in the valence band is calculated using

$$p = \int_{-\infty}^0 DOS_h(E) [1 - f(E)] dE = N_v \mathfrak{F}_{-1/2}(\eta_v) \quad (10)$$

where the effective DOS of holes, N_v and normalised energy in terms of thermal energy, η_v is given by $N_v = \sqrt{(2m_h^* k_B T)/\pi \hbar^2}$ and $\eta_v = (E_v - E_F)/k_B T$ respectively. Note that for holes concentration, $f(E)$ is replaced by $[1 - f(E)]$ to calculate the probability that the states are empty in the valence band.

The FDI can be separated into two regimes, namely non-degenerate and degenerate regimes which reduces (9) into $\mathfrak{F}_j(\eta) = e^\eta$ for $(\eta < -2)$ regardless of j and $\mathfrak{F}_j(\eta) = \eta^{j+1}/[(j+1)\Gamma(j+1)]$ for $(\eta \geq 3)$ respectively [55]. Fig. 5(a) and (b) shows the carrier concentration of electrons and holes respectively for both the exact numerical FDI and reduced FDI calculations. The extracted degenerate carrier concentration for electrons at $\eta_c = 3$ is $n = 1.77 \times 10^8 \text{ m}^{-1}$ and for holes $\eta_v = 3$ is $p = 1.84 \times 10^8 \text{ m}^{-1}$ respectively. At the degenerate regime, the carrier concentrations (both n and p) become saturated and do not vary

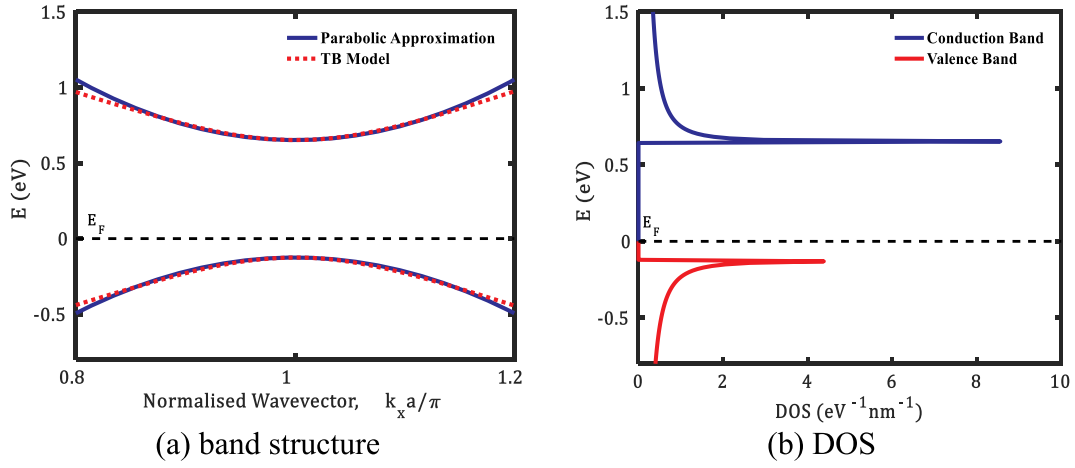


Fig. 4. The band structure and DOS of AlSi₃NW in the zigzag direction using parabolic band assumption.

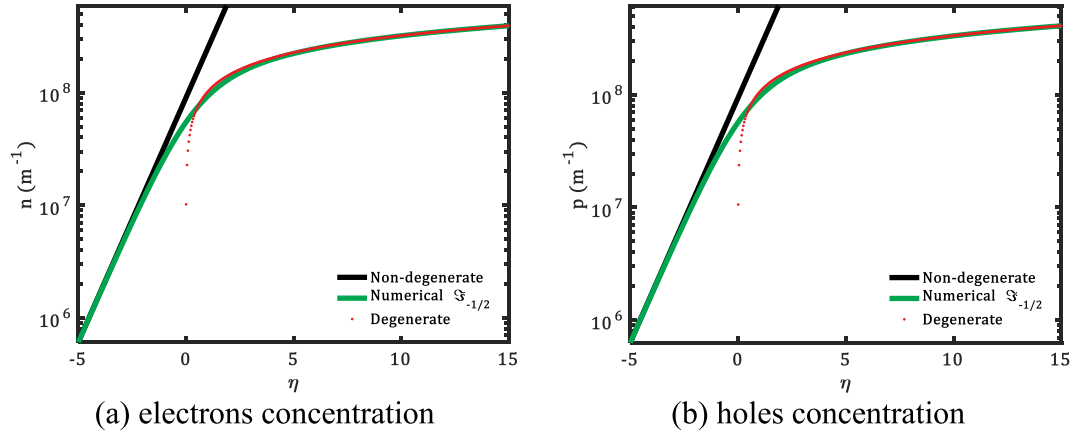


Fig. 5. The carrier concentrations versus the normalised Fermi energy, η within the degenerate and non-degenerate regimes.

significantly.

3. Mathematical modelling for current-voltage characteristics

From this section onwards, the modelling procedure will focus on the carrier transport via the conduction band. This is due to the p-type nature of AlSi₃NW which makes it more suitable to be applied as an n-channel MOSFET which primarily depends on the electrons mobility [56].

3.1. Intrinsic velocity of AlSi₃NW

The intrinsic velocity of electrons can be obtained by dividing the total electrons velocity by the electrons concentration [57] which is expressed as

$$v_{ie} = \frac{\int_0^\infty |v_e(E)| DOS_e(E) f(E) dE}{\int_0^\infty DOS_e(E) f(E) dE} \quad (11)$$

where $|v_e(E)| = \sqrt{2(E - E_c)/m_e^*}$ is the average magnitude of the velocity for electrons. Using (8) and (9), (11) is simplified to become

$$v_{ie} = v_{thn} \frac{\mathfrak{S}_0(\eta_c)}{\mathfrak{S}_{-1/2}(\eta_c)} \quad (12)$$

where $v_{thn} = \sqrt{2k_B T / \pi m_e^*}$ is the thermal velocity of electrons for AlSi₃NW.

Figs. 6 and 7 illustrates the intrinsic velocity of electrons with respect

to temperature and electron concentrations respectively. From Fig. 6, the relationship, $v_{ie} \propto T^{0.5}$ at fixed values of n can be observed. Referring to Fig. 7, the intrinsic velocity is almost constant for non-degenerate regime ($n < 1 \times 10^8 \text{ m}^{-1}$). On the other hand, temperature has almost no effect on v_{ie} at the degenerate regime ($n > 1 \times 10^8 \text{ m}^{-1}$), and v_{ie} has

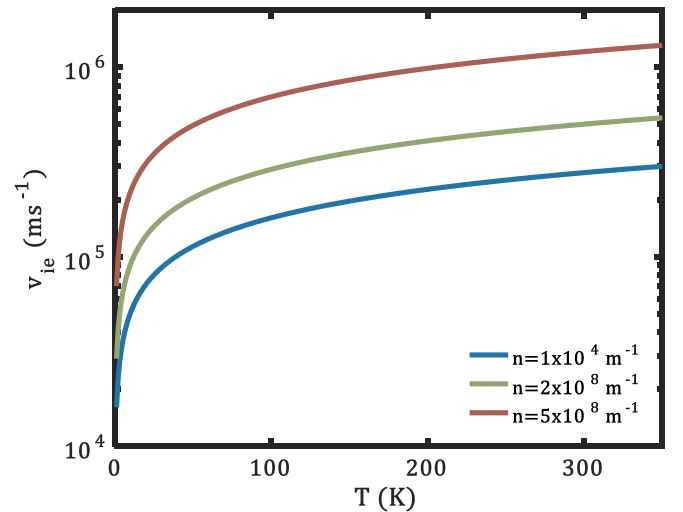


Fig. 6. The intrinsic velocity versus the temperature of AlSi₃NW for various electron concentrations.

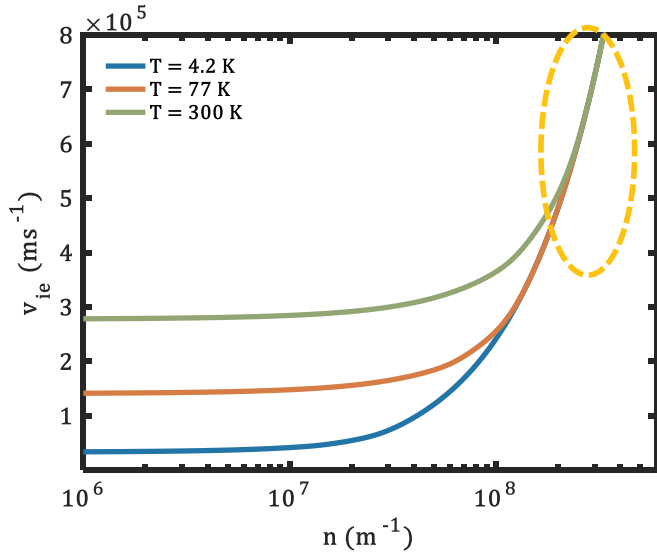


Fig. 7. The intrinsic velocity versus the electron concentration of AlSi₃NW at T = 4.2 K, T = 77 K and T = 300 K (room temperature) respectively. The orange dashed oval shows that the intrinsic velocity is independent of temperature at degenerate regime. (For interpretation of the references to colour in this figure legend, the reader is referred to the Web version of this article.)

simply become a function of carrier concentration only. The independence of temperature at the degenerate regime is in consistent with the results in previous study [58] on 1D device.

3.2. Current-voltage characteristics of AlSi₃NW

For more insights on the carrier flow in the AlSi₃NW by utilising the carrier transport properties obtained in previous subsections, the ballistic current transport is modelled using Landauer-Büttiker current equation. The schematic diagram and energy band diagram of the current transport model is shown in Fig. 8(a) and Fig. 8(b) respectively. A potential within the channel parameter is defined. The potential, $U \equiv -qV_{bias}$ is a potential within the channel which is controlled by the gate voltage in a MOSFET device [59]. Note that the effects of the gate metal work function and oxide permittivity are neglected for simplification and to verify the result of the proposed model with published result [60]. The Landauer-Büttiker ballistic current transport equation [61] incorporating the effect of potential U is given by

$$I_{DS} = \frac{q}{2} \int_0^\infty |v_e(E-U)| DOS_e(E-U) [f_s(E-\mu_s) - f_D(E-\mu_D)] dE \quad (13)$$

where q is the constant for electric charge, f_s and f_D is the Fermi-Dirac

distribution for source and drain respectively. By assuming ideal metal contacts and high drain bias, $f_s(E-\mu_s) \gg f_D(E-\mu_D)$ such that only the carriers with positive velocity would be considered [62] as shown in Fig. 8(b). Moreover, the term U is removed from the velocity and DOS terms and substituted into the Fermi-Dirac probability equation to simplify numerical procedure. Rearranging (13) to obtain

$$I_{DS} = \frac{q}{2} \int_0^\infty |v_e(E)| D(E) f_s(E+U) dE \quad (14)$$

An expression similar to the integral term of (14) is obtained by multiplying (12) with (8). Then, (14) can be expressed as

$$I_{DS} = \frac{qN_c v_{thn} \zeta_0}{2} \left[\frac{E_F + qV_{bias} - E_c}{k_B T} \right] \quad (15)$$

where N_c and v_{thn} are the same parameters as defined in (9) and (12) respectively. Fig. 9 shows the I-V characteristics of AlSi₃NW at T = 300 K plotted using (15). The trend of I-V characteristic is in consistent with the drain current versus gate to source voltage characteristic at fixed drain bias [63].

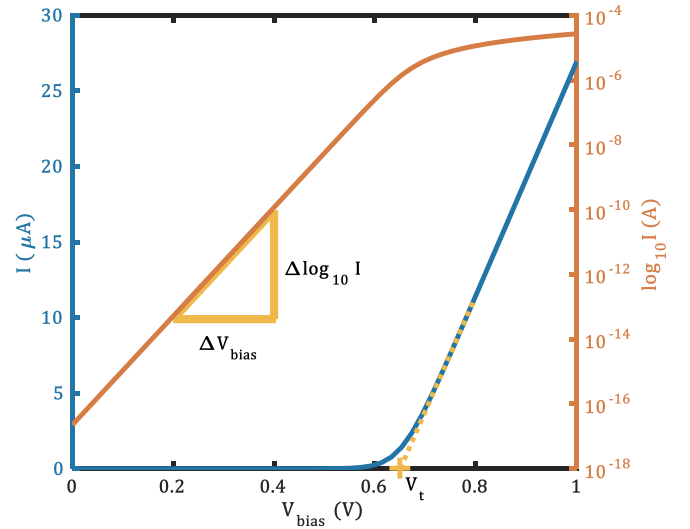


Fig. 9. The I-V characteristics of AlSi₃NW where the blue line and axis indicates the current in the linear scale while the orange line and axis indicates the current in logarithmic scale. The yellow triangle is used to calculate the subthreshold swing (SS) and the yellow cross '+' marks the threshold voltage (V_t). (For interpretation of the references to colour in this figure legend, the reader is referred to the Web version of this article.)

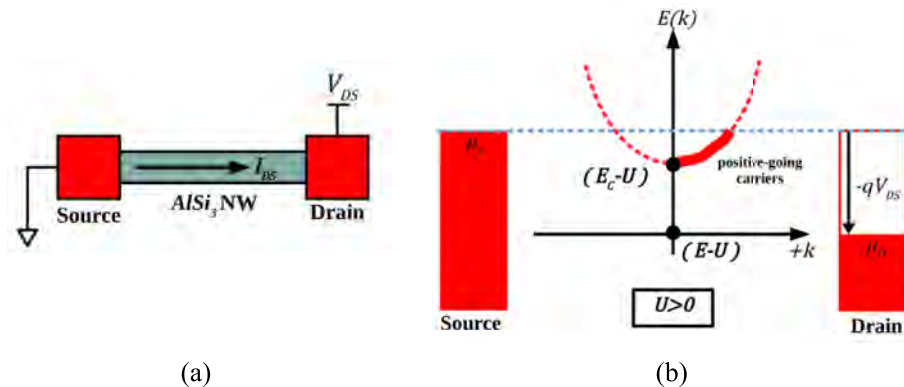


Fig. 8. The current transport model: (a) schematic diagram and (b) the simplified energy band diagram.

4. Discussions

The value of band gap obtained for AlSi_3NW is 0.78 eV which is between the band gap values for widely accepted semiconductors such as germanium which is 0.66 eV and silicon which is 1.12 eV [64]. Thus, these results imply that AlSi_3NW is a prospective material for future nanoelectronic switching devices. From the I-V characteristics in Fig. 9, a very small non-zero off current of the order of 10^{-8} to 10^{-16} at the subthreshold regime can be observed. To further evaluate the I-V characteristics, one of the device performance metrics for MOSFET devices, namely subthreshold swing (SS) [65–67] is evaluated using

$$SS = \frac{\Delta V_{bias}}{\Delta \log_{10} I} \quad (16)$$

where ΔV_{bias} is the difference in biasing voltage in mV and $\Delta \log_{10} I$ is the difference in drain current in the logarithmic scale. The computed SS based on the yellow triangle in Fig. 9 is $SS \approx 60 mV/decade$ which is in consistent with the SS value at room temperature ($T = 300 \text{ K}$) [64]. In addition, the threshold voltage [63] solely based on the channel without the influence of gate parameters is obtained as $V_t = 0.65 V$ as shown in Fig. 9.

Fig. 10 compares the results of proposed AlSi_3NW model with published BC_2NNW model which employs similar modelling approach. Similar to the model in Ref. [60], the model in this work has neglected the effects of gate metal work-function and gate oxide dielectric permittivity to the I-V characteristics. The results show that both structures have achieved the standard $SS \approx 60 mV/decade$ subthreshold conduction. However, the threshold voltage of BC_2NNW is higher than that of AlSi_3NW which implies that lower gate bias is required to turn on the MOSFET device that employ AlSi_3NW as the channel material. Referring to the evidence explained by Lim et al. [60], BC_2NNW is more suitable for sensor applications. These findings further support that the AlSi_3NW is suitable to be applied in MOSFET device. However, the proposed model is the ideal case which requires further investigation as the performance parameters [63] of metal-semiconductor (for source to channel and drain to channel connection) and metal-oxide-semiconductor (for gate to gate oxide and gate oxide to semiconductor) are neglected. For instance, the gate metal work-function can cause deviation to the value of threshold voltage, V_t of the MOSFET devices [68]. The gate oxide material and the effective oxide thickness (EOT) can also affect the performance of the device in terms of leakage current [69]. These issues require further investigation as they are crucial to the device performance.

5. Conclusion

In summary, the proposed model has achieved the objective of the work, that is, to assess the electronic and carrier transport properties of AlSi_3NW . The important properties, namely the electronic band structure, DOS, intrinsic carrier concentration, intrinsic velocity and ideal ballistic I-V characteristics have been described in details. The electronic properties of gapless silicene have been successfully engineered such that semiconducting band gap value of 0.78 eV is obtained. The degenerate electrons and holes concentrations of AlSi_3NW are $n = 1.77 \times 10^8 \text{ m}^{-1}$ and $p = 1.84 \times 10^8 \text{ m}^{-1}$ respectively. In addition, it is observed the intrinsic velocity is proportional to $T^{0.5}$ at non-degenerate regime and independent of temperature at degenerate regime. The I-V characteristics show that AlSi_3NW can achieve SS of $60 mV/decade$ and V_t of $0.65 V$ under ideal conditions at room temperature, indicating good channel control and switching behaviour. The theoretical model reveals that AlSi_3NW is a potential candidate for future nanoelectronic applications. These findings provide insights for future research such as investigating the issues on the properties of metal-semiconductor contacts and metal-oxide-semiconductor contacts.

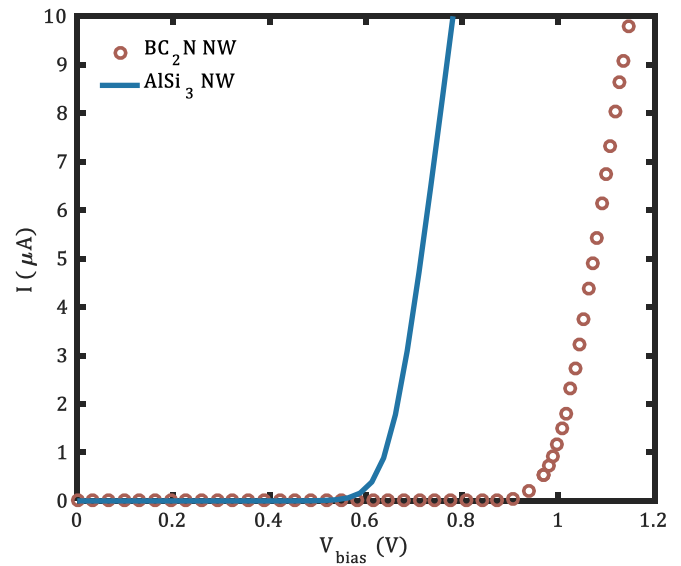


Fig. 10. The comparison of I-V characteristics of AlSi_3NW (blue solid line) of the proposed model and BC_2NNW (red dotted line) adapted from Ref. [60]. (For interpretation of the references to colour in this figure legend, the reader is referred to the Web version of this article.)

Acknowledgements

The authors acknowledge the Research Management Centre (RMC) of Universiti Teknologi Malaysia (UTM) for providing excellent support and conducive research environment. Mu Wen expresses his appreciation for the award of UTM National Postgraduate Fund (NPF) from the School of Graduate Studies UTM. Michael Tan would like to acknowledge the financial support from Fundamental Research Grant Scheme (FRGS) (Vote no.: R.J130000.7851.5F043) that allowed the research to proceed smoothly.

Appendix A. Supplementary data

Supplementary data to this article can be found online at <https://doi.org/10.1016/j.physe.2019.113731>.

References

- [1] M.M. Waldrop, More than Moore, *Nature* 530 (2016) 144–148. <https://doi.org/10.1038/530144a>.
- [2] M. Chhowalla, D. Jena, H. Zhang, Two-dimensional semiconductors for transistors, *Nat. Rev. Mater.* 1 (2016) 16052. <https://www.nature.com/articles/natrevmats201652>.
- [3] P. Ye, T. Ernst, M.V. Khare, The last silicon transistor: nanosheet devices could be the final evolutionary step for Moore's Law, *IEEE Spectr* 56 (2019) 30–35. <https://doi.org/10.1109/MSPEC.2019.8784120>.
- [4] K.S. Novoselov, V. Fal, L. Colombo, P. Gellert, M. Schwab, K. Kim, A roadmap for graphene, *Nature* 490 (2012) 192. <https://doi.org/10.1038/nature11458>.
- [5] K.S. Novoselov, A.K. Geim, S.V. Morozov, D. Jiang, Y. Zhang, S.V. Dubonos, I. V. Grigorieva, A.A. Firsov, Electric field effect in atomically thin carbon films, *Science* 306 (2004) 666–669. <https://doi.org/10.1126/science.1102896>.
- [6] G.R. Bhimanapati, Z. Lin, V. Meunier, Y. Jung, J. Cha, S. Das, D. Xiao, Y. Son, M. S. Strano, V.R. Cooper, Recent advances in two-dimensional materials beyond graphene, *ACS Nano* 9 (2015) 11509–11539. <https://doi.org/10.1021/acsnano.5b05556>.
- [7] M.W. Chuan, K.L. Wong, A. Hamzah, S. Rusli, N.E. Alias, C.S. Lim, M.L.P. Tan, 2D honeycomb silicon: a review on theoretical advances for silicene field-effect transistors, *Curr. Nanosci.* (2019). In press. <https://doi.org/10.2174/1573413715666190709120019>.
- [8] IEEE, International roadmap for devices and Systems (IRDS). <https://irds.ieee.org/>, 2018. (Accessed 28 August 2019).
- [9] K. Takeda, K. Shiraishi, Theoretical possibility of stage corrugation in Si and Ge analogs of graphite, *Phys. Rev. B* 50 (1994) 14916. <https://doi.org/10.1103/PhysRevB.50.14916>.
- [10] S. Cahangirov, M. Topsakal, E. Aktürk, H. Şahin, S. Ciraci, Two- and one-dimensional honeycomb structures of silicon and germanium, *Phys. Rev. Lett.* 102 (2009) 236804. <https://doi.org/10.1103/PhysRevLett.102.236804>.

- [11] G.G. Guzmán-Verri, L.L.Y. Voon, Electronic structure of silicon-based nanostructures, *Phys. Rev. B* 76 (2007), 075131. <https://doi.org/10.1103/PhysRevB.76.075131>.
- [12] L. Tao, E. Cinquanta, D. Chiappe, C. Grazianetti, M. Fanciulli, M. Dubey, A. Molle, D. Akinwande, Silicene field-effect transistors operating at room temperature, *Nat. Nanotechnol.* 10 (2015) 227. <https://doi.org/10.1038/NNANO.2014.325>.
- [13] S. Sadeddine, H. Enriquez, A. Bendounan, P.K. Das, I. Vobornik, A. Kara, A. J. Mayne, F. Sirotti, G. Dujardin, H. Oughaddou, Compelling experimental evidence of a Dirac cone in the electronic structure of a 2D Silicon layer, *Sci. Rep.* 7 (2017) 44400. <https://doi.org/10.1038/srep44400>.
- [14] H.-C. Hsu, Y.-H. Lu, T.-L. Su, W.-C. Lin, T.-Y. Fu, Single crystalline silicene consist of various superstructures using a flexible ultrathin Ag (111) template on Si (111), *Semicond. Sci. Technol.* 33 (2018), 075004. <https://doi.org/10.1088/1361-6641/aaad88>.
- [15] A. Stepniak-Dybala, M. Krawiec, formation of silicene on ultra-thin Pb (111) films, *J. Phys. Chem. C* (2019). <https://doi.org/10.1021/acs.jpcc.9b04343>.
- [16] B. Lalmi, H. Oughaddou, H. Enriquez, A. Kara, S. Vizzini, B. Ealet, B. Aufray, Epitaxial growth of a silicene sheet, *Appl. Phys. Lett.* 97 (2010) 223109. <https://doi.org/10.1063/1.3524215>.
- [17] B. Sarebanha, S. Ahmadi, L. Eslami, Impact of Phosphorus superlattices on charge and spin dependent transport properties of zigzag silicene nanoribbons, *Physica E Low Dimens. Syst. Nanostruct.* 89 (2017) 139–147. <https://doi.org/10.1016/j.physe.2017.02.013>.
- [18] H. Oughaddou, H. Enriquez, M.R. Tchalala, H. Yildirim, A.J. Mayne, A. Bendounan, G. Dujardin, M.A. Ali, A. Kara, Silicene, a promising new 2D material, *Prog. Surf. Sci.* 90 (2015) 46–83. <https://doi.org/10.1016/j.progsurf.2014.12.003>.
- [19] Z. Ni, H. Zhong, X. Jiang, R. Quhe, G. Luo, Y. Wang, M. Ye, J. Yang, J. Shi, J. Lu, Tunable band gap and doping type in silicene by surface adsorption: towards tunneling transistors, *Nanoscale* 6 (2014) 7609–7618. <https://doi.org/10.1039/c4nr00028e>.
- [20] Q. Tang, Z. Zhou, Graphene-analogous low-dimensional materials, *Prog. Mater. Sci.* 58 (2013) 1244–1315. <https://doi.org/10.1016/j.pmatsci.2013.04.003>.
- [21] N. Yin, Y. Dai, W. Wei, B. Huang, Electronic structure engineering in silicene via atom substitution and a new two-dimensional Dirac structure Si₃C, *Physica E Low Dimens. Syst. Nanostruct.* 98 (2018) 39–44. <https://doi.org/10.1016/j.physe.2017.12.024>.
- [22] H. Zheng, Z. Wang, T. Luo, Q. Shi, J. Chen, Analytical study of electronic structure in armchair graphene nanoribbons, *Phys. Rev. B* 75 (2007) 165414. <https://doi.org/10.1103/PhysRevB.75.165414>.
- [23] S. Cahangirov, M. Topsakal, S. Ciraci, Armchair nanoribbons of silicon and germanium honeycomb structures, *Phys. Rev. B* 81 (2010) 195120. <https://doi.org/10.1103/PhysRevB.81.195120>.
- [24] S. Trivedi, A. Srivastava, R. Kurchania, Electronic and transport properties of silicene nanoribbons, *J. Comput. Theor. Nanosci.* 11 (2014) 789–794. <https://doi.org/10.1166/jctn.2014.3429>.
- [25] J. Gao, J. Zhang, H. Liu, Q. Zhang, J. Zhao, Structures, mobilities, electronic and magnetic properties of point defects in silicene, *Nanoscale* 5 (2013) 9785–9792. <https://doi.org/10.1039/c3nr02826g>.
- [26] R. Li, Y. Han, T. Hu, J. Dong, Y. Kawazoe, Self-healing monovacancy in low-buckled silicene studied by first-principles calculations, *Phys. Rev. B* 90 (2014), 045425. <https://doi.org/10.1103/PhysRevB.90.045425>.
- [27] M. Ali, X. Pi, Y. Liu, D. Yang, Electronic and magnetic properties of graphene, silicene and germanene with varying vacancy concentration, *AIP Adv.* 7 (2017), 045308. <https://doi.org/10.1063/1.4980836>.
- [28] K. Iordanidou, M. Houssa, B. van den Broek, G. Pourtois, V. Afanas'ev, A. Stesmans, Impact of point defects on the electronic and transport properties of silicene nanoribbons, *J. Phys. Condens. Matter* 28 (2016), 035302. <https://doi.org/10.1088/0953-8984/28/3/035302>.
- [29] S. Mehdi Aghaei, I. Calizo, Band gap tuning of armchair silicene nanoribbons using periodic hexagonal holes, *J. Appl. Phys.* 118 (2015) 104304. <https://doi.org/10.1063/1.4930139>.
- [30] A.A. Fouladi, Electronic transport properties of T-shaped silicene nanoribbons, *Physica E Low Dimens. Syst. Nanostruct.* 91 (2017) 101–105. <https://doi.org/10.1016/j.physe.2016.10.040>.
- [31] D. Ghosh, P. Parida, S.K. Pati, Stable line defects in silicene, *Phys. Rev. B* 92 (2015) 195136. <https://doi.org/10.1103/PhysRevB.92.195136>.
- [32] A. Lopez-Bezanilla, Substitutional doping widens silicene gap, *J. Phys. Chem. C* 118 (2014) 18788–18792. <https://doi.org/10.1021/jp5060809>.
- [33] L. Ma, J.-M. Zhang, K.-W. Xu, V. Ji, Nitrogen and Boron substitutional doped zigzag silicene nanoribbons: Ab initio investigation, *Physica E Low Dimens. Syst. Nanostruct.* 60 (2014) 112–117. <https://doi.org/10.1016/j.physe.2014.02.013>.
- [34] Y. Pogorelov, V. Loktev, Biased doped silicene as a way to tune electronic conduction, *Phys. Rev. B* 93 (2016), 045117. <https://doi.org/10.1103/PhysRevB.93.045117>.
- [35] J. Chen, X.F. Wang, P. Vasilopoulos, A.B. Chen, J.C. Wu, Single and multiple doping effects on charge transport in zigzag silicene nanoribbons, *ChemPhysChem* 15 (2014) 2701–2706. <https://doi.org/10.1002/cphc.201402171>.
- [36] Y. Ding, Y. Wang, Density functional theory study of the silicene-like SiX and XSi₃ (X = B, C, N, Al, P) honeycomb lattices: the various buckled structures and versatile electronic properties, *J. Phys. Chem. C* 117 (2013) 18266–18278. <https://doi.org/10.1021/jp407666m>.
- [37] B. Mohan, A. Kumar, P. Ahluwalia, Electronic and optical properties of silicene under uni-axial and bi-axial mechanical strains: a first principle study, *Physica E Low Dimens. Syst. Nanostruct.* 61 (2014) 40–47. <https://doi.org/10.1016/j.physe.2014.03.013>.
- [38] H. Zhao, Strain and chirality effects on the mechanical and electronic properties of silicene and silicane under uniaxial tension, *Phys. Lett. A* 376 (2012) 3546–3550. <https://doi.org/10.1016/j.physleta.2012.10.024>.
- [39] B.-H. Kim, M. Park, G. Kim, K. Hermansson, P. Broqvist, H.-J. Choi, K.-R. Lee, Indirect-to-Direct band gap transition of Si nanosheets: effect of biaxial strain, *J. Phys. Chem. C* 122 (2018) 15297–15303. <https://doi.org/10.1021/acs.jpcc.8b02239>.
- [40] N. Ding, H. Wang, X. Chen, C.-M.L. Wu, Defect-sensitive performance of silicene sheets under uniaxial tension: mechanical properties, electronic structures and failure behavior, *RSC Adv.* 7 (2017) 10306–10315. <https://doi.org/10.1039/c6ra27291f>.
- [41] N. Wang, H. Guo, Y.-j. Liu, J.-x. Zhao, Q.-h. Cai, X.-z. Wang, Asymmetric functionalization as a promising route to open the band gap of silicene: a theoretical prediction, *Physica E Low Dimens. Syst. Nanostruct.* 73 (2015) 21–26. <https://doi.org/10.1016/j.physe.2015.05.014>.
- [42] Y. Ding, Y. Wang, Hydrogen-induced stabilization and tunable electronic structures of penta-silicene: a computational study, *J. Phys. Chem. C* 3 (2015) 11341–11348. <https://doi.org/10.1039/c5tc02504d>.
- [43] Y. Ding, Y. Wang, Tunable electronic structures of hydrogenated zigzag and armchair dumbbell silicene nanosheets: a computational study, *J. Phys. Chem. C* 122 (2018) 23208–23216. <https://doi.org/10.1021/acs.jpcc.8b08268>.
- [44] Y. Taur, Y.-J. Mii, D.J. Frank, H.-S. Wong, D.A. Buchanan, S.J. Wind, S.A. Rishton, G. Sai-Halasz, E.J. Nowak, CMOS scaling into the 21st century: 0.1 μm and beyond, *IBM J. Res. Dev.* 39 (1995) 245–260. <https://doi.org/10.1147/rd.391.0245>.
- [45] S. Datta, Quantum Transport: Atom to Transistor, Cambridge university press, 2005. <https://doi.org/10.1017/CBO9781139164313>.
- [46] W.A. Harrison, Elementary Electronic Structure: Revised, World Scientific Publishing Company, 2004. <https://doi.org/10.1142/5432>.
- [47] W.H. Lim, A. Hamzah, M.T. Ahmadi, R. Ismail, Band gap engineering of BC2N for nanoelectronic applications, *Superlattice Microstruct.* 112 (2017) 328–338. <https://doi.org/10.1016/j.spmi.2017.09.040>.
- [48] M.S. Lundstrom, D.A. Antoniadis, Compact models and the physics of nanoscale FETs, *IEEE Trans. Electron Devices* 61 (2013) 225–233. <https://doi.org/10.1109/TED.2013.2283253>.
- [49] R. Ismail, M.T. Ahmadi, S. Anwar, Advanced Nanoelectronics, CRC Press, 2016. <https://doi.org/10.1201/9781315217185>.
- [50] S. Datta, Electronic Transport in Mesoscopic Systems, Cambridge university press, 1997. <https://doi.org/10.1017/CBO9780511805776>.
- [51] W.H. Lim, A. Hamzah, M.T. Ahmadi, R. Ismail, Analytical study of the electronic properties of boron nitride nanosheet, in: 2017 IEEE Regional Symposium on Micro and Nanoelectronics (RSM), IEEE, 2017, pp. 42–45. <https://doi.org/10.1109/RSM.2017.8069115>.
- [52] M. Lundstrom, C. Jeong, Near-Equilibrium Transport: Fundamentals and Applications, World Scientific Publishing Company, 2012. <https://doi.org/10.1142/7975>.
- [53] M.K.Q. Jooq, A. Mir, S. Mirzakuchaki, A. Farmani, Semi-analytical modeling of high performance nano-scale complementary logic gates utilizing ballistic carbon nanotube transistors, *Physica E Low Dimens. Syst. Nanostruct.* 104 (2018) 286–296. <https://doi.org/10.1016/j.physe.2018.08.008>.
- [54] R. Kim, M. Lundstrom, Notes on Fermi-Dirac Integrals, third ed., 2008. <https://nanohub.org/resources/5475>.
- [55] Z. Johari, M.T. Ahmadi, D.C.Y. Chek, N.A. Amin, R. Ismail, Modelling of graphene nanoribbon Fermi energy, *J. Nanomater.* 2010 (2010) 14. <https://doi.org/10.1155/2010/909347>.
- [56] M. Md Arshad, N. Othman, U. Hashim, Fully depletion of advanced silicon on insulator MOSFETs, *Crit. Rev. Solid State Mater. Sci.* 40 (2015) 182–196. <https://doi.org/10.1080/10408436.2014.978447>.
- [57] V.K. Arora, Nanoelectronics: Quantum Engineering of Low-Dimensional Nanoensembles, CRC Press, 2015. <https://doi.org/10.1201/b18131>.
- [58] M.T. Ahmadi, H.H. Lau, R. Ismail, V.K. Arora, Current-voltage characteristics of a silicon nanowire transistor, *Microelectron. J.* 40 (2009) 547–549. <https://doi.org/10.1016/j.mejo.2008.06.060>.
- [59] M. Lundstrom, Z. Ren, Essential physics of carrier transport in nanoscale MOSFETs, *IEEE Trans. Electron Devices* 49 (2002) 133–141. <https://doi.org/10.1109/16.974760>.
- [60] W.H. Lim, A. Hamzah, M.T. Ahmadi, R. Ismail, Performance analysis of one dimensional BC2N for nanoelectronics applications, *Physica E Low Dimens. Syst. Nanostruct.* 102 (2018) 33–38. <https://doi.org/10.1016/j.physe.2018.04.005>.
- [61] A. Rahman, J. Guo, S. Datta, M.S. Lundstrom, Theory of ballistic nanotransistors, *IEEE Trans. Electron Devices* 50 (2003) 1853–1864. <https://doi.org/10.1109/9/TED.2003.815366>.
- [62] D. Supriyo, Lessons from Nanoelectronics: A New Perspective on Transport -Part A: Basic Concepts, World Scientific, 2017. <https://doi.org/10.1142/10440>.
- [63] M. Lundstrom, J. Guo, Nanoscale Transistors: Device Physics, Modeling and Simulation, Springer Science & Business Media, 2006. <https://doi.org/10.1007/0-387-28003-0>.
- [64] D.A. Neamen, Semiconductor Physics and Devices: Basic Principles, McGraw-Hill, New York, NY, 2012. [http://refhub.elsevier.com/S1386-9477\(18\)30117-6/sref48](http://refhub.elsevier.com/S1386-9477(18)30117-6/sref48).
- [65] H.C. Chin, C.S. Lim, W.S. Wong, K.A. Danapalasingam, V.K. Arora, M.L.P. Tan, Enhanced device and circuit-level performance benchmarking of graphene nanoribbon field-effect transistor against a nano-MOSFET with interconnects, *J. Nanomater.* 2014 (2014). <https://doi.org/10.1155/2014/879813>.
- [66] N. Ghoabi, M. Pourfath, A comparative study of tunneling FETs based on graphene and GNR heterostructures, *IEEE Trans. Electron Devices* 61 (2013) 186–192. <https://doi.org/10.1109/TED.2013.2291788>.

- [67] A. Nazari, R. Faez, H. Shamloo, Modeling comparison of graphene nanoribbon field effect transistors with single vacancy defect, *Superlattice Microstruct.* 97 (2016) 28–45. <https://doi.org/10.1016/j.spmi.2016.06.008>.
- [68] J. Franco, Z. Wu, G. Rzepa, L.-A. Ragnarsson, H. Dekkers, A. Vandooren, G. Groeseneken, N. Horiguchi, N. Collaert, D. Linten, On the impact of the gate work-function metal on the charge trapping component of NBTI and PBTI, *IEEE Trans. Device Mater. Reliab.* 19 (2019) 268–274. <https://doi.org/10.1109/TDMR.2019.2913258>.
- [69] C.-H. Dai, T.-C. Chang, A.-K. Chu, Y.-J. Kuo, S.-H. Ho, T.-Y. Hsieh, W.-H. Lo, C.-E. Chen, J.-M. Shih, W.-L. Chung, Hot carrier effect on gate-induced drain leakage current in high-k/metal gate n-channel metal-oxide-semiconductor field-effect transistors, *Appl. Phys. Lett.* 99 (2011), 012106. <https://doi.org/10.1063/1.3608241>.